Weak H-Bond Interface Environment for Stable Aqueous Zinc Batteries

Shuai Wang,[a,b] Haoran Wang,[a] Jiguo Tu,[c] Lei Huang,[a] Shenzhen Deng,[b] Bingang Xu,[b,*] and Lei Wei[a,*]

[a]School of Electrical and Electronic Engineering, Nanyang Technological University, Singapore 639798, Singapore

[b]Nanotechnology Center, School of Fashion and Textiles, The Hong Kong Polytechnic University, Hung Hom, Kowloon, Hong Kong 999077, China

[c]School of Chemistry, Chemical Engineering and Biotechnology, Nanyang Technological University, Singapore 639798, Singapore

E-mails: wei.lei@ntu.edu.sg; tcxubg@polyu.edu.hk

Keywords: weak H-bond interface, suspension electrolyte, strong polarity, hydroxyl functional group, enhanced performance

Abstract: Hydrogen evolution reaction and Zn dendrite growth, originated from high water activity and the adverse competition between the electrochemical kinetics and mass transfer, are the main constraints for the commercial applications of the aqueous zinc-based batteries. Herein, a weak H-bond interface with suspension electrolyte is developed by adding TiO_2 nanoparticles into the electrolytes. Owing to the strong polarity of Ti-O bonds in TiO_2, abundant hydroxyl functional groups are formed between the $TiO_{2[110]}$ active surface and aqueous environment, which can produce a weak H-bond interface by disrupting the initial H-bond networks between the water molecules, thereby accelerating the mass transfer of Zn^{2+} and reducing the water activity. In consequence, the Zn||Zn symmetrical cells display reversible Zn plating/stripping behaviors with a high Coulombic efficiency of 99.7% over 700 cycles. Moreover, the TiO_2-based suspension strategy is also applicable to other zinc salt systems and exhibits fast plating/stripping behaviors. The suspension electrolyte enables long-term life full cells including Zn||PANI hybrid capacitors and Zn||ZnVO full batteries.

INTRODUCTION

Rechargeable aqueous zinc batteries (RAZBs) have the intrinsic features of relatively low cost, high safety, and environmental benignity,[1-4] demonstrating highly promising for large-scale energy storage devices.[5-8] As a common anode material in RAZBs, Zn metal possesses the advantages of low redox potential, large capacity, and high compatibility with aqueous electrolytes.[9-10] However, the long-standing obstacles to the practical commercialization of RAZBs lie in the side-reactions, dendrite growth, and hydrogen evolution reaction (HER) that occur on the Zn surface,[11-12] causing a low Coulombic efficiency (CE) and inferior reversibility of Zn metal.[13-14] Even worse, the dendritic deposited Zn with irregular morphology may puncture the separator and cause a quick fail of the cell.[15-16] Hence, optimizing the reaction interface between the electrode and electrolyte in terms of component and structure is vital to guide the uniform Zn deposition and suppress the HER.[17-19]

Various strategies have been attempted to solve the problems associated with Zn anodes, mainly including electrolyte engineering,[20-27] artificial interface,[28-32] and structure optimization.[33-38] Notably, the electrolyte engineering emerges as a particularly accessible aspect of battery manufacturing, making it exceptionally appealing.[39-41] More importantly, electrolyte engineering through the introduction of organic molecules or inorganic salts into the electrolytes has been verified to enhance the stability of Zn metal.[40, 42] For instance, the majority of electrolyte engineering strategies are centered around tuning the solvation structure of Zn^{2+} hydration ($[Zn(H_2O)_6]^{2+}$), which can alter the solvation structures and reduce the water activity in the solvation structures, thus impeding the HER and side reactions.[43-44] Moreover, the regulation of hydrated Zn^{2+} can improve the kinetics of the Zn^{2+} de-solvation process and uniformize the nucleation sites of Zn^{2+}, thus inducing uniform Zn^{2+} deposition to alleviate the dendrite growth.[45-46] However, despite significant endeavors that have been dedicated to the advanced aqueous electrolytes for RAZBs through the perspective of electrolyte engineering strategies, there are still key unresolved issues regarding the intricate correlation between the

reaction interphase and Zn stability. In fact, the ions plating process follows a competing mechanism between electrochemical reaction and mass transfer.[47-48] The fast kinetic reaction leads to the preferential deposition of ions in certain tip regions, resulting in the formation of dendrites. Subsequently, the ions are unable to immediately migrate to the reaction interface due to the sluggish mass transfer, further accelerating the dendrite growth. In addition, the hydrogen bond (H-bond) networks between the water molecules can diminish their stability to a certain extent, thus promoting the HER.[49] However, the electrochemical reaction is difficult to be further improved by simple electrolyte engineering strategies. Therefore, designing an aqueous electrolyte that can simultaneously enhance the mass transfer and reduce the water activity is important to further improve the electrochemical performance.

Herein, we propose a weak H-bond interface with suspension electrolyte by mixing titanium dioxide (TiO_2) nanoparticles with the liquid electrolytes to elucidate the interface's roles in enhancing the reversibility of the Zn anode (Scheme 1a). At the oxides/water molecules contact interface, abundant hydroxyl functional groups are generated on the $TiO_{2[110]}$ active surface due to the strong polarity of Ti-O bonds in TiO_2, which can construct a network of weak H-bond interface capable of rapidly transporting Zn^{2+} by accelerating the mass transfer of water molecules at the reaction interface (Scheme 1b). Moreover, the interfacial field between the TiO_2 surface and water molecules can further break the H-bond networks between the water molecules to reduce the water activity. Hence, the suspension electrolyte can simultaneously homogenize Zn^{2+} deposition and suppress the HER. On the basis of these advantages, the Zn anodes in the suspension electrolyte achieve a long lifespan and high Coulombic efficiency. Moreover, the corresponding hybrid capacitors and full batteries demonstrate superior rate capability and excellent cycling stability.

RESULTS AND DISCUSSION

TiO_2 nanoparticles, as a typical polar oxide, were selected to be introduced in the liquid electrolytes to generate the suspension electrolytes (Figures S1a and S2a). In this study, silicon dioxide (SiO_2) nanoparticles were selected to construct a reference suspension electrolyte due to the weak polarity of Si-O bonds in SiO_2 (Figures S1b and S2b). SiO_2 and TiO_2-based suspension electrolytes are regarded as sus-SiO_2 and sus-TiO_2 electrolytes, respectively. Generally, the existence of hydroxyl functional groups on the oxide surfaces can improve their bonding properties and surface characteristics.[50-51] As shown in Figure 1a, owing to the small size and the electrostatic repulsive effect between the oxides with the same charge, nano-sized oxides (0.05 *wt*.%) can be uniformly dispersed in the aqueous electrolytes with obvious Tyndall phenomenon. Even after standing for 12 hours, the sus-TiO_2 electrolyte can still maintain a stable dispersity owing to its higher Zeta potential value than the sus-SiO_2 electrolyte (Figures S3 and S4). Moreover, the ionic conductivities of various electrolytes were calculated to be about ~25-30 mS cm^{-1} (Figure 1b), suggesting that a slight addition of nano-sized oxides has an insignificant impact on the ionic conductivity of the electrolytes. However, we have found that the suspension dispersity is not too uniform when the content of oxides reaches 0.1 *wt*.% (Figures S5 and S6). Furthermore, the ionic conductivities of the suspension electrolytes with high concentrations drop to low values (Figure S7), which will hinder the ion migration in electrolytes during the reaction process. Therefore, 0.05 *wt*.% oxides are considered as the optimal content for suspension electrolytes and have been employed to evaluate the electrochemical properties of suspension electrolytes.

Fourier transform infrared (FTIR) spectra of the various electrolytes were conducted to verify the influence of nano-sized oxides on the evolution of H-bond networks between the water molecules. In the FTIR spectra (Figure 1c and Figure S8), there is no significant difference after adding SiO_2 nanoparticles into the liquid electrolyte. Nevertheless, the peaks of O-H bending vibrations (1,634 cm^{-1}) and O-H stretches (3,200-3,400 cm^{-1}) exhibit a blueshift in the sus-TiO_2 electrolyte, demonstrating that H-bond networks between $TiO_{2[110]}$ active

surface and water molecules are strengthened while the initial H-bond networks between the water molecules are weakened. This variation is ascribed to the bond interactions between water molecules and oxides, which can also be confirmed by Raman and nuclear magnetic resonance (NMR). Owing to the different H-bond environments, the O-H vibration peaks (3,100-3,700 cm^{-1}) can be fitted into three regions, including strong, medium, and weak H-bond regions (Figure S9a).[52] Compared with the liquid electrolyte, the ratio of strong H-bond in the sus-TiO_2 electrolyte decreases from 33.41% to 25.25% due to the re-construction of H-bond networks under the influence of hydroxylated TiO_2 (Figure S9b).[52] In the NMR spectra, the peaks of ^{1}H and ^{17}O resonances experience an upshift in the sus-TiO_2 electrolyte (Figure 1d and Figure S10), indicating a diminished electronic density of H and O atoms caused by the charge transfer between Ti-O bond in TiO_2 and O-H bond in H_2O due to the strong polarity of Ti-O bonds.[52-53] Furthermore, the relaxation dynamics evolution of water molecules was analyzed by the 2D low-field NMR (LF-NMR) spectra.[54] The time regions (T_2) in the range of ~100-500 ms and ~1,000 ms are attributed to the immobilized water and free water, respectively.[55] Significant immobilized water molecules are found in the sus-TiO_2 electrolyte (Figure 1f), suggesting that the number of H-bond between the water molecules can be markedly reduced due to the introduction of TiO_2 nanoparticles. In contrast, almost only free water molecules are observed in the liquid and sus-SiO_2 electrolytes while the proportion of immobilized water molecules can be neglected (Figure 1e and Figure S11). These findings demonstrate that the bond interactions between water molecules and oxides can effectively break the original H-bond networks among the water molecules, stiffen the O-H bond and soften the O:H bond (Figure 1g), which is also confirmed by the crystal orbital overlap population (COOP) of O-H bonds in the water molecule networks (Figure S12).

Next, the interactions between the TiO_2 active surface and water molecule were explored by density functional theory (DFT) calculations (Figure 1h,i, Figures S13 and S14). Figure 1h shows the different structural geometries (G_1, G_2, and G_3) of the $TiO_{2[110]}$ active surface during

the hydroxylation process. G_1 corresponds to the original adsorbed water molecule near the $TiO_{2[110]}$ surface, G_2 represents the formation of two hydroxyl groups on the $TiO_{2[110]}$ active surface after the dehydrogenation process, and G_3 exhibits a fully dissociative water geometry. The charge density difference maps show the charge redistributions in these geometries (Figure 1h, below), basically reflecting the evolution process of the hydroxyl groups on the $TiO_{2[110]}$ surface,[56] which is consistent with the results from NMR (Figure 1d and Figure S10). However, the calculated energy barrier from G_2 to G_3 is much higher than that from G_1 to G_2, and the electronic excitation can reach up to 4.59 eV (Figure 1i), indicating that G_3 does not exist theoretically. That is to say, the hydroxylation process on the $TiO_{2[110]}$ active surface originates from the first step of dehydrogenation of water molecules near its surface. Furthermore, the pH values of the various electrolytes were tested to evaluate the hydroxylation process. As shown in Figure S15, the addition of nano-TiO_2 to the liquid electrolyte increases the pH values from 3.84 to 4.16, indicating that some free hydroxyl groups are formed during the hydroxylation process. This process can effectively reduce the number of free H^+ ions and prevent anodic corrosion compared to the liquid electrolyte. To deeply gain insight into the modification mechanisms of various suspension electrolytes, the disparities of H-bonds between the interfacial and internal water molecules were investigated by molecular dynamics (MD) simulations (Figure 1j and Figure S16). In these models, the oxide surfaces were fully mobile throughout the simulations. The real electrolyte compositions (including water molecules, OTf^- and Zn^{2+} ions) were added in the *z*-direction of oxide active surfaces, as illustrated in Table S1. Radial distribution functions (RDFs) show that abundant O_{oxide}-H coordination structures (coordination distance: ~0.97 Å) appear on the $TiO_{2[110]}$ surface (Figure S17), confirming the existence of -OH groups on its surface.[57] In contrast, only a few O_{oxide}-H coordination structures are observed on the $SiO_{2[101]}$ surface owing to the weak polarity of Si-O bonds.[58] Such distinction endows the $TiO_{2[110]}$ surface with more H-bond networks. As shown in Figure 1k, the mean value of H-bonds per unit area is ~0.30 on its surface, which is much higher than that

(0.25) on the $SiO_{2[101]}$ surface. Moreover, a precise analysis of the H-bond distributions was performed to acquire the H-bond evolution in terms of length and angle (Figure 1l and Figure S18).

As discussed above, the water activity is effectively restrained in the sus-TiO_2 electrolyte. Consequently, the HER potential presents a negative shift of ~10 mV in the sus-TiO_2 electrolyte than the liquid and sus-SiO_2 electrolytes (Figure 2a), indicating that the renormalized H-Bond networks can suppress the HER. Moreover, Tafel curves were performed to evaluate the anticorrosion capability of various electrolytes (Figure 2b and Figure S19). Herein, the calculated corrosion current density and potential of Zn metal in the sus-TiO_2 electrolyte are 0.10 mA cm^{-2} and -0.85 V, respectively. These values are much lower than the cases in both liquid and sus-SiO_2 electrolytes. Accordingly, the Zn anode in the sus-TiO_2 electrolyte has better thermodynamic stability,[59-60] verified by the optical images of soaked Zn metal in various electrolytes after 10 days (Figure S20). Furthermore, the electric double layer (EDL) capacitance tests were investigated through the cyclic voltammetry (CV) curves to confirm the adsorption phenomenon of nano-TiO_2 on the Zn anode (Figure S21), which is also identified by the X-ray photoelectron spectroscopy (XPS) results (Figure S22). In the CV curves, Zn||Zn cell exhibits a lower EDL capacitance of ~0.155 mF cm^{-2} in the sus-TiO_2 electrolyte than that in the $Zn(OTf)_2$ electrolyte. The reduction of the EDL capacitance in the sus-TiO_2 electrolyte can be attributed to the formation of an adsorption layer near the Zn anode.[49, 61] The potential impact of nano-TiO_2 on the electrode's EDL structure may provide insight into the uniform electric field observed during the Zn plating/stripping process, as well as the enhanced Zn^{2+} diffusion kinetics. The nucleation behaviors of Zn^{2+} ions in various electrolytes were analyzed using the chronoamperometry test at a constant overpotential of -150 mV (Figure 2c). In the liquid and sus-SiO_2 electrolytes, the currents continuously rise within 500 s, suggesting a 2D diffusion process along the metal surface in which Zn^{2+} ions easily deposit at a certain tip region and gradually evolve into the dendrites.[62] A stable 3D diffusion process with a low and smooth

current rapidly occurs after a transient 2D diffusion process in the sus-TiO_2 electrolyte, facilitating the formation of smooth deposited Zn.[63] As a result, the Zn^{2+} transference number in the sus-TiO_2 electrolyte (0.71) is much higher than the cases (0.48 and 0.37) of the liquid and sus-SiO_2 electrolytes (Figure 2d and Figure S23). Meanwhile, the sus-TiO_2 electrolyte with a weak H-bond interface endows Zn^{2+} ions with lower nucleation overpotential and faster reaction kinetics during the Zn plating process (Figure 2e,f and Figure S24). MD simulations were further performed to quantify the dynamic relaxation behaviors of the water molecules. Dipole vector autocorrelation function (DACF) was plotted for the interfacial and internal water molecules (Figure 2g). The relaxation rate of the interfacial water molecules on the $TiO_{2[110]}$ surface is much faster than the interfacial water molecules on the $SiO_{2[101]}$ surface and internal water molecules. A faster relaxation rate indicates a more energetic molecule kinetics process, which is related to the negative of the derivative of $C_{\mu\mu}$.[64] The kinetics of interfacial water molecules in the sus-TiO_2 electrolyte likely accelerates because the interfacial field breaks the original H-bond networks. The dynamic relaxation behaviors were also verified by the self-diffusion coefficient of the water molecules (Figure 2h), which is consistent with the DACF results. Consequently, the water molecules on the $TiO_{2[110]}$ surface possess high mean local diffusion coefficients in all directions (Figure 2i), meaning the increase in the mass transfer of Zn^{2+}.

The symmetric Zn||Zn cells were utilized to illustrate the reversibility of Zn in various electrolytes. As evidenced in Figure 3a and Figure S25, the cells with the liquid and sus-SiO_2 electrolytes display drastically fluctuating signals due to battery failure,[65] while the Zn||Zn cell of sus-TiO_2 electrolyte delivers a satisfactory average CE of 99.5% after 700 cycles at 1.0 mA cm^{-2}. A high average CE of 99.7% is still achieved even at a large current density of 5.0 mA cm^{-2} (Figure S26), reflecting the excellent reversibility of Zn in such a suspension electrolyte. Notably, the comprehensive properties of Zn anode in the suspension electrolyte, including high CE, high current density, and long-term cycle number, outperform many published Zn anodes

(Figure 3b),[52, 66-74] implying the superiority of our strategy for the RAZBs. The fast ion transfer kinetics in the sus-TiO_2 electrolyte endows the Zn anode with satisfying rate capability (Figure 3c). A lower overpotential could always be obtained in the case of using the sus-TiO_2 electrolyte as the current density increases from 0.5 to 30 mA cm^{-2} (Figure 3d), profiting from the stable reaction interface and favorable Zn^{2+} conduction (Figure 3e). Encouragingly, the low overpotentials at high current densities are far exceeding the values of many reported literature (Figure S27). Furthermore, the Zn||Zn cell with the sus-TiO_2 electrolyte exhibits a long-term lifespan (1,500 h at 3.0 mA cm^{-2}) with a stable overpotential (Figure 3f). However, the cells with liquid and sus-SiO_2 electrolytes fail after less than 100 h, possibly due to the uncontrolled Zn dendrite-induced short circuits.[75] For the high areal capacity in the Zn||Zn cell with the sus-TiO_2 electrolyte, the cell can still be stably cycled for 160 h at a high Zn utilization rate of ~85.5% and a high current density of 15 mA cm^{-2} (Figure S28). In addition, the shelving-recovery tests were carried out to assess the practical conditions of RAZBs. The Zn||Zn cells was operated with an intermittent discharge/charge test (Figure 3g). Noticeably, the Zn||Zn cell operates stably over 600 h in the sus-TiO_2 electrolyte, whereas the cells with liquid and sus-SiO_2 electrolytes can only run less than 200 h due to the formation of side reactants and Zn dendrites. The morphology evolution of Zn anodes after cycling in various electrolytes was disclosed by scanning electron microscopy (SEM) and optical images (Figure 3h and Figure S29). After cycling, the Zn anodes with the liquid and sus-SiO_2 electrolytes deliver a dendrite-like structure with different sizes, which can easily trigger cell failure. For the Zn anode with the sus-TiO_2 electrolyte, no discernible dendrites are observed on its surface after cycling, implying the notable influence of nano-sized TiO_2 on the Zn deposition process. More importantly, the TiO_2-based suspension strategy could be extended to other zinc salt electrolyte systems, such as $ZnSO_4$ and $ZnClO_4$-based aqueous electrolytes (Figures S30-S36), greatly enhancing its commercial value. The Zn||Zn cells with the TiO_2-based suspension electrolytes exhibit a long-term lifespan of 1,500 h at 3.0 mA cm^{-2} with a stable overpotential (Figure S32).

SEM images of Zn anodes after multiple cycles are shown to illustrate the Zn deposition process in these TiO_2-based suspension electrolytes (Figure S33). Obviously, almost no dendrites are observed on the Zn surface, suggesting the superiority of suspension electrolyte on regulation of Zn deposition. Furthermore, we assembled the different types of full batteries to assess the reliability of the TiO_2-based suspension electrolyte (Figures S34-S36). The Zn||PANI hybrid capacitors and Zn||ZVO full batteries exhibit high capacity and excellent stability after thousands of cycles. Impressively, the Zn||I_2 full battery with a high mass loading (8.0 mg cm^{-2}) delivers over 4,000 stable cycling (2.0 A g^{-1}) with only ~11% capacity loss.

The Zn nucleation behaviors in various electrolytes were evaluated by different spectroscopic techniques. In the X-ray diffraction (XRD) patterns (Figure 4a), a higher value (0.64) of I_{002}/I_{101} of deposited Zn is achieved in the sus-TiO_2 electrolyte as compared to the cases in the other electrolytes. The surface orientation of deposited Zn was also elucidated using the wide-angle X-ray scattering (WAXS) patterns (Figure 4b,c and Figure S37), where the signals of deposited $Zn_{[002]}$ in the sus-TiO_2 electrolyte are more recognizable as compared to the signals in the other electrolytes. These results verify that the sus-TiO_2 electrolyte can guide the Zn deposition along the $Zn_{[002]}$ plane to restrain the formation of by-products and dendrites, thus achieving stable Zn anodes.[76-77] Atomic force microscope (AFM) images discover the nucleation morphologies of deposited Zn in various electrolytes (Figure 4d). After cycling, the Zn anode reflects a glabrous surface in the sus-TiO_2 electrolyte, while the rough surfaces with larger protuberances occur in the liquid and sus-SiO_2 electrolytes. The corresponding surface roughness was further acquired from the statistical results to show the differences between the deposited Zn surfaces in various electrolytes, confirming the superiority of the sus-TiO_2 electrolyte on Zn nucleation behaviors (Figure S38). Furthermore, to observe the *in-situ* Zn deposition behaviors, we constructed two types of operando optical detection platforms from both cross-sectional and planar directions (Figure 4e and Figure S39). In the cross-sectional optical images, the Zn dendrites begin to generate from 10 min and reach about 50-120 μm after

60 min in the liquid and sus-SiO_2 electrolytes (Figure 4f and Figure S40). By contrast, no evident protuberances are observed on the Zn deposition layer in the sus-TiO_2 electrolyte (Figure 4g). The similar Zn deposition behaviors were also verified through the *in-situ* planar optical images (Figure S41).

Finally, hybrid capacitors based on polyaniline (PANI) cathodes were assembled to illustrate the practical feasibility of the sus-TiO_2 electrolyte (Figure S42). Figure 5a compares the rate capability of Zn||PANI hybrid capacitors in various electrolytes. As expected, the sus-TiO_2 electrolyte endows the Zn||PANI hybrid capacitor with high capacities at all current densities. Moreover, the capacity can recover to the initial value of ~100 mAh g^{-1} as the current density turns back to 0.2 A g^{-1} (Figure 5b), exhibiting an excellent rate capability. This is attributed to the advanced interfacial reaction kinetics in the sus-TiO_2 electrolyte in comparison with other electrolytes (Figure 5c and Figure S43). 2D CV patterns were also conducted to illustrate the electrochemical process of Zn (Figure 5d,e and Figure S44). The potential of the cathodic peak (peak A) gets significantly increased due to the small charge transfer resistance in the sus-TiO_2 electrolyte (Figure 5c), which helps contribute to higher output voltage and energy density. The reaction kinetics of the cells are understood by CV curves and ion diffusion coefficient (*D*). For instance, with the increase of scan rates from 0.2 to 1.0 mV s^{-1}, the current intensities of redox peaks are gradually enhanced (Figure S45). The capacitive contribution of the cell based on the sus-TiO_2 electrolyte rises gradually and finally reaches ~82.94%, which is higher than the cases of $Zn(OTf)_2$ and sus-SiO_2 electrolytes. This characteristic is favorable for the fast ion diffusion kinetics. Galvanostatic intermittent titration technique (GITT) measurement is further carried out to reveal the ion diffusion coefficient (*D*) (Figure S46). The *D* value with sus-TiO_2 electrolyte determined by GITT is as high as ~10^{-9} to 10^{-10} cm^2 s^{-1}, which can endow the cell with the enhanced reaction kinetics. Besides, Zn||PANI hybrid capacitor with the sus-TiO_2 electrolyte exhibits a long-term cycling behavior over 2,500 cycles (capacity retention: 97.3%), as shown in Figure 5f,g, surpassing the values of capacity retention in other

electrolytes. In the self-discharge assessment, the Zn||PANI hybrid capacitor in the sus-TiO_2 electrolyte demonstrates a lower self-discharging rate, maintaining a voltage of 1.21 V over 24 h, far better than the cases in the liquid and sus-SiO_2 electrolytes (Figure S47). To illustrate the Zn deposition process, the SEM images of Zn anodes after cycling are shown in Figure S48. In the $Zn(OTf)_2$ and sus-SiO_2 electrolytes, the surface is covered with flake-like dendrites or corrosion pits owing to the uneven plating/stripping behaviors. In the sus-TiO_2 electrolyte, no discernible dendrites or pits were observed on the surface of Zn anode after cycling, implying the notable influence of nano-sized TiO_2 on the Zn deposition process. For further practical application evaluation of the sus-TiO_2 electrolyte, $Zn_{0.25}V_2O_5 \cdot H_2O$ and iodine inorganic active cathodes were also selected to assess the electrochemical properties of Zn||ZnVO and Zn||I_2 full batteries (Figure 5h,i and Figures S49-S51). The Zn||ZnVO full battery with sus-TiO_2 electrolyte delivers a high capacity of ~200 mAh g^{-1} and exhibits outstanding stability over 1,000 cycles at 3.0 A g^{-1}. Impressively, the Zn||I_2 full battery with a high mass loading of ~8.0 mg cm^{-2} displays a stable capacity (>120 mAh g^{-1}) over 4,000 cycles at 2.0 A g^{-1}. Hence, the sus-TiO_2 electrolyte endows the RAZBs with enhanced electrochemical properties.

CONCLUSIONS

In summary, we demonstrated that the concept of suspension electrolyte strategy is applicable to the aqueous electrolytes and has broad applicability. Owing to the strong polarity of the Ti-O bonds in TiO_2, the suspended TiO_2 nanoparticles in the sus-TiO_2 electrolyte could disrupt the H-bond networks among the water molecules, thus weakening the water activity to inhibit the HER. Besides, a weak H-bond region was constructed at the electrode/electrolyte interface, accelerating the mass transfer of water molecule, and enhancing the Zn^{2+} transfer kinetics. Therefore, the issues of HER and dendrites on the Zn anode were inhibited in the sus-TiO_2 electrolyte. As a result, the reversibility of Zn plating/stripping was enhanced, which endows Zn anodes with a high average CE of 99.7% after 700 cycles and a stable cycling over 1,500 h at 3mA cm^{-2}. Furthermore, the assembled Zn||PANI hybrid capacitors and Zn||ZnVO full

batteries delivered improved electrochemical performance in the sus-TiO_2 electrolyte. More importantly, the concept of suspension electrolytes in this work could be also extended to other Zn salt-based aqueous electrolytes and might also be helpful for other rechargeable batteries.

METHODS

Synthesis of ZnVO Microspheres. ZnVO microspheres were prepared by a microwave hydrothermal method. Typically, 0.36 g of vanadium pentoxide (V_2O_5, 99.6%, Aladdin) and 0.38 g of zinc acetate dihydrate ($Zn(CH_3COO)_2{\cdot}2H_2O$, 99%, Sigma-Aldrich) were dispersed in a 50 mL mixed solution (acetone/water, mass ratio: 1:15) and stirred for 5 h. Then, the above solution was transferred into a Teflon-lined autoclave and kept at 180 ºC for 1.5 h. The obtained dark orange powder was washed with deionized water many times and dried at 60 ºC overnight.

Preparation of Suspension Electrolytes and Electrodes. The liquid electrolyte was prepared by dissolving 10.9 g of zinc trifluoromethanesulfonate ($Zn(OTf)_2$, 98%, Sigma-Aldrich) in 10 ml of deionized water. The SiO_2 and TiO_2 suspension electrolytes (regarded as sus-SiO_2 and sus-TiO_2 electrolytes) were prepared by mixing indicated amount (0.05 and 0.1 *wt*.%) of nanoparticles (Nano SiO_2, diameter: ~50-150 nm; Nano TiO_2, diameter: ~50-100 nm, Sigma-Aldrich) with liquid electrolyte (3M $Zn(OTf)_2$). The suspension electrolytes were strongly ultrasonic stirred for 2 h.

To prepare the polyaniline (PANI, 98%, Macklin) and ZnVO cathodes, PANI or ZnVO powders, Ketjen black, and polyvinylidene fluoride (PVDF, Aladdin) in a weight ratio of 8:1:1 were mixed in N-methyl-2-pyrrolidone (NMP, 99.5%, Aladdin) solvent. The slurry was coated on stainless-steel meshes (diameter: 12 mm) and dried under vacuum at 80 °C for 24 h to remove the residual solvent. The mass loading of the active materials on the cathodes was around 1.0-1.5 mg cm^{-2}, and the thickness of the cathode was ~60 μm. Zn, Ti, and Cu foils (thickness: 50 μm, Shengshida Metal Materials Co., LTD) were cut into small disks (diameter: 12 mm) and then cleaned with deionized water and ethanol in sequence before use. For the high

areal capacity in the symmetrical cell tests, the thickness of Zn foil was ~30 μm, corresponding to a theoretical capacity of about 17.55 mAh cm^{-2}.

Preparation of High Mass Loading I_2@Ac Cathode. The I_2@Ac composite was fabricated using a melt-diffusion method. Typically, active carbon (Ac) and I_2, in a mass ratio of 1:9, were thoroughly mixed by hand grinding for 10 mins. Subsequently, the mixture was sealed in a glass bottle and heated at 80°C for 6 h. For the preparation of I_2@Ac cathodes, a slurry was prepared by mixing the I_2@Ac composite (80%), Ketjen black (10%), and PVDF binder (10%) in NMP. Then, the slurry was uniformly coated on a carbon cloth (CC) and dried at 50°C overnight. The areal mass loading of I_2 in the cathodes was controlled at ~8.0 mg cm^{-2}.

ASSOCIATED CONTENT

Supporting Information

The Supporting Information is available free of charge at https://pubs.acs.org.

Experimental details for the materials used in the experiment, characterizations, electrochemical measurements, FTIR spectra and TEM images of TiO_2 and SiO_2 nanoparticles, digital images and Tyndall effect, the statistical Zeta potentials of the various electrolytes, Nyquist impedance plots and the corresponding ionic conductivities, NMR spectra of various electrolytes, 2D LF-NMR T_1-T_2 relaxation spectra of the various electrolytes, the crystal orbital overlap population (COOP) of O-H bonds, XRD patterns, structural geometry, snapshot of MD simulation, the probability of H-bond length, the corrosive currents and potentials, optical images of soaked Zn metal in the various electrolytes, current-time plots of Zn||Zn symmetric cells, CV curves of Zn||Ti cells, voltage-capacity curves, CE tests of Zn||Cu cells, rate capability of Zn||Zn cells, long-term cycle performance of Zn||Zn cells, WAXS pattern of the deposited Zn, 2D AFM images of the deposited Zn surface, schematic diagram of *in-situ* optical detection platform, *in-situ* optical images of Zn plating, characterizations of PANI powders, 2D contour plots of

CV patterns of Zn||PANI hybrid capacitors, characterizations of ZnVO cathode materials, and the sizes of MD simulation systems.

AUTHOR INFORMATION

Corresponding Authors

Lei Wei-School of Electrical and Electronic Engineering, Nanyang Technological University, Singapore 639798, Singapore

E-mail: wei.lei@ntu.edu.sg

Bingang Xu-Nanotechnology Center, School of Fashion and Textiles, The Hong Kong Polytechnic University, Hung Hom, Kowloon, Hong Kong 999077, China

E-mail: tcxubg@polyu.edu.hk

Authors

Shuai Wang-School of Electrical and Electronic Engineering, Nanyang Technological University, Singapore 639798, Singapore; Nanotechnology Center, School of Fashion and Textiles, The Hong Kong Polytechnic University, Hung Hom, Kowloon, Hong Kong 999077, China

Haoran Wang-School of Electrical and Electronic Engineering, Nanyang Technological University, Singapore 639798, Singapore

Lei Huang-School of Electrical and Electronic Engineering, Nanyang Technological University, Singapore 639798, Singapore

Jiguo Tu-School of Chemistry, Chemical Engineering and Biotechnology, Nanyang Technological University, Singapore 639798, Singapore

Shenzhen Deng-Nanotechnology Center, School of Fashion and Textiles, The Hong Kong Polytechnic University, Hung Hom, Kowloon, Hong Kong 999077, China

Author Contributions

S.W. and L.W. conceived the research. S.W. designed and performed the experiments. H.-R.W. and J.T. conducted the material synthesis and structure characterizations. L.H. and S.-Z.D. assisted with the data

analysis. S.W. and H.-R.W. performed the electrochemical measurements of cells. S.W. performed the MD simulations and DFT calculations and wrote the paper. L.W. and B.-G.X. supervised the research and revised the paper. All authors discussed the results.

Notes

The authors declare no competing financial interest.

ACKNOWLEDGEMENTS

This work was supported by the Singapore Ministry of Education Academic Research Fund Tier 2 (MOE2019-T2-2-127, MOE-T2EP50120-0002 and MOE-T2EP50123-0014), the Singapore Ministry of Education Academic Research Fund Tier 1 (RG62/22), A*STAR under AME IRG (A2083c0062), A*STAR under IAF-ICP Programme I2001E0067 and the Schaeffler Hub for Advanced Research at NTU, the IDMxS (Institute for Digital Molecular Analytics and Science) by the Singapore Ministry of Education under the Research Centres of Excellence scheme, and the NTU-PSL Joint Lab collaboration. The authors would like to thank Shiyanjia Lab (www.shiyanjia.com) for the LF-NMR analysis.

REFERENCES

(1) Cao, L.; Li, D.; Pollard, T.; Deng, T.; Zhang, B.; Yang, C.; Chen, L.; Vatamanu, J.; Hu, E.; Hourwitz, M. J.; Ma, L.; Ding, M.; Li, Q.; Hou, S.; Gaskell, K.; Fourkas, J. T.; Yang, X.-Q.; Xu, K.; Borodin, O.; Wang, C. Fluorinated interphase enables reversible aqueous zinc battery chemistries. *Nat. Nanotechnol.* **2021,** *16*, 902-910.

(2) Yang, C.; Xia, J.; Cui, C.; Pollard, T. P.; Vatamanu, J.; Faraone, A.; Dura, J. A.; Tyagi, M.; Kattan, A.; Thimsen, E.; Xu, J.; Song, W.; Hu, E.; Ji, X.; Hou, S.; Zhang, X.; Ding, M. S.; Hwang, S.; Su, D.; Ren, Y.; Yang, X.-Q.; Wang, H.; Borodin, O.; Wang, C. All-temperature zinc batteries with high-entropy aqueous electrolyte. *Nat. Sustain.* **2023,** *6*, 325-335.

(3) Yang, X.; Li, C.; Sun, Z.; Yang, S.; Shi, Z.; Huang, R.; Liu, B.; Li, S.; Wu, Y.; Wang, M.; Su, Y.; Dou, S.; Sun, J. Interfacial manipulation via in situ grown ZnSe cultivator toward highly reversible Zn metal anodes. *Adv. Mater.* **2021,** *33*, 2105951.

(4) Yang, J.-L.; Liu, H.-H.; Zhao, X.-X.; Zhang, X.-Y.; Zhang, K.-Y.; Ma, M.-Y.; Gu, Z.-Y.; Cao, J.-M.; Wu, X.-L. Janus Binder chemistry for synchronous enhancement of iodine species adsorption and redox kinetics toward sustainable aqueous Zn-I_2 batteries. *J. Am. Chem. Soc.* **2024,** *146*, 6628-6637.

(5) Zhu, Z.; Jiang, T.; Ali, M.; Meng, Y.; Jin, Y.; Cui, Y.; Chen, W. Rechargeable batteries for grid scale energy storage. *Chem. Rev.* **2022,** *122*, 16610-16751.

(6) Chao, D.; Zhou, W.; Xie, F.; Ye, C.; Li, H.; Jaroniec, M.; Qiao, S.-Z. Roadmap for advanced aqueous batteries: From design of materials to applications. *Sci. Adv.* **2020,** *6*, eaba4098.

(7) Liang, G.; Tang, Z.; Han, B.; Zhu, J.; Chen, A.; Li, Q.; Chen, Z.; Huang, Z.; Li, X.; Yang, Q.; Zhi, C. Regulating inorganic and organic components to build amorphous-ZnF_x enriched solid-electrolyte interphase for highly reversible Zn metal chemistry. *Adv. Mater.* **2023,** *35*, 2210051.

(8) Heng, Y.; Gu, Z.; Guo, J.; Wu, X. Research progresses on vanadium-based cathode materials for aqueous zinc-ion batteries. *Acta Phys. -Chim. Sin.* **2020,** *37*, 2005013.

(9) Wang, R.; Yao, M.; Yang, M.; Zhu, J.; Chen, J.; Niu, Z. Synergetic modulation on ionic association and solvation structure by electron-withdrawing effect for aqueous zinc-ion batteries. *Proc. Natl. Acad. Sci. USA* **2023,** *120*, e2221980120.

(10) Geng, L.; Meng, J.; Wang, X.; Han, C.; Han, K.; Xiao, Z.; Huang, M.; Xu, P.; Zhang, L.; Zhou, L.; Mai, L. Eutectic electrolyte with unique solvation structure for high-performance zinc-ion batteries. *Angew. Chem. Int. Ed.* **2022,** *61*, e202206717.

(11) Zhong, C.; Liu, B.; Ding, J.; Liu, X.; Zhong, Y.; Li, Y.; Sun, C.; Han, X.; Deng, Y.; Zhao, N.; Hu, W. Decoupling electrolytes towards stable and high-energy rechargeable aqueous zinc-manganese dioxide batteries. *Nat. Energy* **2020,** *5*, 440-449.

(12) Wang, D.; Lv, D.; Liu, H.; Zhang, S.; Wang, C.; Wang, C.; Yang, J.; Qian, Y. In situ formation of nitrogen-rich solid electrolyte interphase and simultaneous regulating

solvation structures for advanced Zn metal batteries. *Angew. Chem. Int. Ed.* **2022,** *61*, e202212839.

(13) Zhang, Q.; Luan, J.; Tang, Y.; Ji, X.; Wang, H. Interfacial design of dendrite-free zinc anodes for aqueous zinc-ion batteries. *Angew. Chem. Int. Ed.* **2020,** *59*, 13180-13191.

(14) Li, H.; Zhao, R.; Zhou, W.; Wang, L.; Li, W.; Zhao, D.; Chao, D. Trade-off between zincophilicity and zincophobicity: toward stable Zn-based aqueous batteries. *JACS Au* **2023,** *3*, 2107-2116.

(15) Zhao, R.; Wang, H.; Du, H.; Yang, Y.; Gao, Z.; Qie, L.; Huang, Y. Lanthanum nitrate as aqueous electrolyte additive for favourable zinc metal electrodeposition. *Nat. Commun.* **2022,** *13*, 3252.

(16) Zheng, J.; Zhao, Q.; Tang, T.; Yin, J.; Quilty, C. D.; Renderos, G. D.; Liu, X.; Deng, Y.; Wang, L.; Bock, D. C.; Jaye, C.; Zhang, D.; Takeuchi, E. S.; Takeuchi, K. J.; Marschilok, A. C.; Archer, L. A. Reversible epitaxial electrodeposition of metals in battery anodes. *Science* **2019,** *366*, 645-648.

(17) Mu, Y.; Li, Z.; Wu, B.-k.; Huang, H.; Wu, F.; Chu, Y.; Zou, L.; Yang, M.; He, J.; Ye, L.; Han, M.; Zhao, T.; Zeng, L. 3D hierarchical graphene matrices enable stable Zn anodes for aqueous Zn batteries. *Nat. Commun.* **2023,** *14*, 4205.

(18) He, X.; Cui, Y.; Qian, Y.; Wu, Y.; Ling, H.; Zhang, H.; Kong, X.-Y.; Zhao, Y.; Xue, M.; Jiang, L.; Wen, L. Anion concentration gradient-assisted construction of a solid-electrolyte interphase for a stable zinc metal anode at high rates. *J. Am. Chem. Soc.* **2022,** *144*, 11168-11177.

(19) Naveed, A.; Yang, H.; Shao, Y.; Yang, J.; Yanna, N.; Liu, J.; Shi, S.; Zhang, L.; Ye, A.; He, B.; Wang, J. A highly reversible Zn anode with intrinsically safe organic electrolyte for long-cycle-life batteries. *Adv. Mater.* **2019,** *31*, 1900668.

(20) Zhang, Q.; Ma, Y.; Lu, Y.; Li, L.; Wan, F.; Zhang, K.; Chen, J. Modulating electrolyte structure for ultralow temperature aqueous zinc batteries. *Nat. Commun.* **2020,** *11*, 4463.

(21) Shi, X.; Xie, J.; Wang, J.; Xie, S.; Yang, Z.; Lu, X. A weakly solvating electrolyte towards practical rechargeable aqueous zinc-ion batteries. *Nat. Commun.* **2024,** *15*, 302.

(22) Wang, F.; Borodin, O.; Gao, T.; Fan, X.; Sun, W.; Han, F.; Faraone, A.; Dura, J. A.; Xu, K.; Wang, C. Highly reversible zinc metal anode for aqueous batteries. *Nat. Mater.* **2018,** *17*, 543-549.

(23) Xu, W.; Li, J.; Liao, X.; Zhang, L.; Zhang, X.; Liu, C.; Amine, K.; Zhao, K.; Lu, J. Fluoride-rich, organic-inorganic gradient interphase enabled by sacrificial solvation shells for reversible zinc metal batteries. *J. Am. Chem. Soc.* **2023,** *145*, 22456-22465.

(24) Ma, L.; Pollard, T. P.; Zhang, Y.; Schroeder, M. A.; Ding, M. S.; Cresce, A. V.; Sun, R.; Baker, D. R.; Helms, B. A.; Maginn, E. J.; Wang, C.; Borodin, O.; Xu, K. Functionalized phosphonium cations enable zinc metal reversibility in aqueous electrolytes. *Angew. Chem. Int. Ed.* **2021,** *60*, 12438-12445.

(25) Zhao, J.; Zhang, J.; Yang, W.; Chen, B.; Zhao, Z.; Qiu, H.; Dong, S.; Zhou, X.; Cui, G.; Chen, L. "Water-in-deep eutectic solvent" electrolytes enable zinc metal anodes for rechargeable aqueous batteries. *Nano Energy* **2019,** *57*, 625-634.

(26) Yang, W.; Du, X.; Zhao, J.; Chen, Z.; Li, J.; Xie, J.; Zhang, Y.; Cui, Z.; Kong, Q.; Zhao, Z.; Wang, C.; Zhang, Q.; Cui, G. Hydrated eutectic electrolytes with ligand-oriented solvation shells for long-cycling zinc-organic batteries. *Joule* **2020,** *4*, 1557-1574.

(27) Tan, H.; Meng, C.; Sun, T.; Wu, X. L.; Liu, H.; Wang, J. J. Boosting zinc anode durability through synergistic inner Helmholtz plane and interfacial electric field regulation. *Sci. Bull.* **2024,** *69*, 2025-2029.

(28) Zheng, X.; Liu, Z.; Sun, J.; Luo, R.; Xu, K.; Si, M.; Kang, J.; Yuan, Y.; Liu, S.; Ahmad, T.; Jiang, T.; Chen, N.; Wang, M.; Xu, Y.; Chuai, M.; Zhu, Z.; Peng, Q.; Meng, Y.; Zhang, K.; Wang, W.; Chen, W. Constructing robust heterostructured interface for anode-free zinc batteries with ultrahigh capacities. *Nat. Commun.* **2023,** *14*, 76.

(29) Wei, S.; Qi, Z.-H.; Xia, Y.; Chen, S.; Wang, C.; Wang, Y.; Zhang, P.; Zhu, K.; Cao, Y.; Guo, X.; Yang, X.; Cui, Q.; Liu, X.; Wu, X.; Song, L. Monolayer thiol engineered covalent interface toward stable zinc metal anode. *ACS Nano* **2022,** *16*, 21152-21162.

(30) Yang, J.; Wang, S.; Du, L.; Bi, S.; Zhu, J.; Liu, L.; Niu, Z. Thermal-cyclized polyacrylonitrile artificial protective layers toward stable zinc anodes for aqueous zinc-based batteries. *Adv. Funct. Mater.* **2024,** *34*, 2314426.

(31) Li, C.; Shyamsunder, A.; Hoane, A. G.; Long, D. M.; Kwok, C. Y.; Kotula, P. G.; Zavadil, K. R.; Gewirth, A. A.; Nazar, L. F. Highly reversible Zn anode with a practical areal capacity enabled by a sustainable electrolyte and superacid interfacial chemistry. *Joule* **2022,** *6*, 1103-1120.

(32) Zhao, R.; Yang, J.; Han, X.; Wang, Y.; Ni, Q.; Hu, Z.; Wu, C.; Bai, Y. Stabilizing Zn metal anodes via cation/anion regulation toward high energy density Zn-ion batteries. *Adv. Energy Mater.* **2023,** *13*, 2203542.

(33) Yu, H.; Zeng, Y.; Li, N. W.; Luan, D.; Yu, L.; Lou, X. W. Confining Sn nanoparticles in interconnected N-doped hollow carbon spheres as hierarchical zincophilic fibers for dendrite-free Zn metal anodes. *Sci. Adv.* **2022,** *8*, eabm5766.

(34) Li, C.; Xie, X.; Liu, H.; Wang, P.; Deng, C.; Lu, B.; Zhou, J.; Liang, S. Integrated 'all-in-one' strategy to stabilize zinc anodes for high-performance zinc-ion batteries. *Natl. Sci. Rev.* **2022,** *9*, nwab177.

(35) Zeng, Y.; Zhang, X.; Qin, R.; Liu, X.; Fang, P.; Zheng, D.; Tong, Y.; Lu, X. Dendrite-free zinc deposition induced by multifunctional cnt frameworks for stable flexible Zn-ion batteries. *Adv. Mater.* **2019,** *31*, 1903675.

(36) Gao, Y.; Cao, Q.; Pu, J.; Zhao, X.; Fu, G.; Chen, J.; Wang, Y.; Guan, C. Stable Zn anodes with triple gradients. *Adv. Mater.* **2023,** *35*, 2207573.

(37) Zhang, G.; Zhang, X.; Liu, H.; Li, J.; Chen, Y.; Duan, H. 3D-printed multi-channel metal lattices enabling localized electric-field redistribution for dendrite-free aqueous Zn ion batteries. *Adv. Energy Mater.* **2021,** *11*, 2003927.

(38) Liang, G.; Zhu, J.; Yan, B.; Li, Q.; Chen, A.; Chen, Z.; Wang, X.; Xiong, B.; Fan, J.; Xu, J.; Zhi, C. Gradient fluorinated alloy to enable highly reversible Zn-metal anode chemistry. *Energy Environ. Sci.* **2022,** *15*, 1086-1096.

(39) Ma, L.; Vatamanu, J.; Hahn, N. T.; Pollard, T. P.; Borodin, O.; Petkov, V.; Schroeder, M. A.; Ren, Y.; Ding, M. S.; Luo, C.; Allen, J. L.; Wang, C.; Xu, K. Highly reversible Zn metal anode enabled by sustainable hydroxyl chemistry. *Proc. Natl. Acad. Sci. USA* **2022,** *119*, e2121138119.

(40) Guo, S.; Qin, L.; Zhang, T.; Zhou, M.; Zhou, J.; Fang, G.; Liang, S. Fundamentals and perspectives of electrolyte additives for aqueous zinc-ion batteries. *Energy Storage Mater.* **2021,** *34*, 545-562.

(41) Meng, C.; He, W.; Jiang, L.; Huang, Y.; Zhang, J.; Liu, H.; Wang, J.-J. Ultra-stable aqueous zinc batteries enabled by β-cyclodextrin: preferred zinc deposition and suppressed parasitic reactions. *Adv. Funct. Mater.* **2022,** *32*, 2207732.

(42) Cao, J.; Zhang, D.; Zhang, X.; Zeng, Z.; Qin, J.; Huang, Y. Strategies of regulating Zn^{2+} solvation structures for dendrite-free and side reaction-suppressed zinc-ion batteries. *Energy Environ. Sci.* **2022,** *15*, 499-528.

(43) Chen, S.; Ji, D.; Chen, Q.; Ma, J.; Hou, S.; Zhang, J. Coordination modulation of hydrated zinc ions to enhance redox reversibility of zinc batteries. *Nat. Commun.* **2023,** *14*, 3526.

(44) Zhang, Q.; Ma, Y.; Lu, Y.; Ni, Y.; Lin, L.; Hao, Z.; Yan, Z.; Zhao, Q.; Chen, J. Halogenated Zn^{2+} solvation structure for reversible Zn metal batteries. *J. Am. Chem. Soc.* **2022,** *144*, 18435-18443.

(45) Sun, P.; Ma, L.; Zhou, W.; Qiu, M.; Wang, Z.; Chao, D.; Mai, W. Simultaneous regulation on solvation shell and electrode interface for dendrite-free Zn ion batteries achieved by a low-cost glucose additive. *Angew. Chem. Int. Ed.* **2021,** *60*, 18247-18255.

(46) Yuan, L.; Hao, J.; Kao, C.-C.; Wu, C.; Liu, H.-K.; Dou, S.-X.; Qiao, S.-Z. Regulation methods for the Zn/electrolyte interphase and the effectiveness evaluation in aqueous Zn-ion batteries. *Energy Environ. Sci.* **2021,** *14*, 5669-5689.

(47) Liu, J.; Bao, Z.; Cui, Y.; Dufek, E. J.; Goodenough, J. B.; Khalifah, P.; Li, Q.; Liaw, B. Y.; Liu, P.; Manthiram, A.; Meng, Y. S.; Subramanian, V. R.; Toney, M. F.; Viswanathan, V. V.; Whittingham, M. S.; Xiao, J.; Xu, W.; Yang, J.; Yang, X.-Q.; Zhang, J.-G. Pathways for practical high-energy long-cycling lithium metal batteries. *Nat. Energy* **2019,** *4*, 180-186.

(48) Xiao, J. How lithium dendrites form in liquid batteries. *Science* **2019,** *366*, 426-427.

(49) Xu, J.; Lv, W.; Yang, W.; Jin, Y.; Jin, Q.; Sun, B.; Zhang, Z.; Wang, T.; Zheng, L.; Shi, X.; Sun, B.; Wang, G. In situ construction of protective films on Zn metal anodes via natural protein additives enabling high-performance zinc ion batteries. *ACS Nano* **2022,** *16*, 11392-11404.

(50) Deng, R.; Chen, J.; Chu, F.; Qian, M.; He, Z.; Robertson, A. W.; Maier, J.; Wu, F. "Soggy-sand" chemistry for high-voltage aqueous zinc-ion batteries. *Adv. Mater.* **2023,** *36*, 2311153.

(51) Das, S. K.; Bhattacharyya, A. J. Oxide particle surface chemistry and ion transport in "soggy sand" electrolytes. *J. Phys. Chem. C* **2009,** *113*, 6699-6705.

(52) Shen, Z.; Mao, J.; Yu, G.; Zhang, W.; Mao, S.; Zhong, W.; Cheng, H.; Guo, J.; Zhang, J.; Lu, Y. Electrocrystallization regulation enabled stacked hexagonal platelet growth toward highly reversible zinc anodes. *Angew. Chem. Int. Ed.* **2023,** *62*, e202218452.

(53) Mattioli, G.; Filippone, F.; Caminiti, R.; Amore Bonapasta, A. Short hydrogen bonds at the water/TiO_2 (anatase) interface. *J. Phys. Chem. C* **2008,** *112*, 13579-13586.

(54) Qiu, M.; Sun, P.; Han, K.; Pang, Z.; Du, J.; Li, J.; Chen, J.; Wang, Z. L.; Mai, W. Tailoring water structure with high-tetrahedral-entropy for antifreezing electrolytes and energy storage at −80 °C. *Nat. Commun.* **2023,** *14*, 601.

(55) Huang, S.; Hou, L.; Li, T.; Jiao, Y.; Wu, P. Antifreezing hydrogel electrolyte with ternary hydrogen bonding for high-performance zinc-ion batteries. *Adv. Mater.* **2022,** *34*, 2110140.

(56) Tan, S.; Feng, H.; Zheng, Q.; Cui, X.; Zhao, J.; Luo, Y.; Yang, J.; Wang, B.; Hou, J. G. Interfacial hydrogen-bonding dynamics in surface-facilitated dehydrogenation of water on TiO_2(110). *J. Am. Chem. Soc.* **2020,** *142*, 826-834.

(57) English, N. J.; Kavathekar, R. S.; MacElroy, J. M. D. Hydrogen bond dynamical properties of adsorbed liquid water monolayers with various TiO_2 interfaces. *Mol. Phys.* **2012,** *110*, 2919-2925.

(58) Massoud, H. Z. Charge-transfer dipole moments at the Si-SiO_2 interface. *J. Appl. Phys.* **1988,** *63*, 2000-2005.

(59) Deng, Q.; You, S.; Min, W.; Xu, Y.; Lin, W.; Lu, J.; Yang, C. Polymer molecules adsorption-induced zincophilic-hydrophobic protective layer enables highly stable Zn metal anodes. *Adv. Mater.* **2024,** *36*, 2312924.

(60) Li, J.; Zhou, S.; Chen, Y.; Meng, X.; Azizi, A.; He, Q.; Li, H.; Chen, L.; Han, C.; Pan, A. Self-smoothing deposition behavior enabled by beneficial potential compensating for highly reversible Zn-metal anodes. *Adv. Funct. Mater.* **2023,** *33*, 2307201.

(61) Zhou, T.; Mu, Y.; Chen, L.; Li, D.; Liu, W.; Yang, C.; Zhang, S.; Wang, Q.; Jiang, P.; Ge, G.; Zhou, H. Toward stable zinc aqueous rechargeable batteries by anode morphology modulation via polyaspartic acid additive. *Energy Storage Mater.* **2022,** *45*, 777-785.

(62) Xie, D.; Sang, Y.; Wang, D.-H.; Diao, W.-Y.; Tao, F.-Y.; Liu, C.; Wang, J.-W.; Sun, H.-Z.; Zhang, J.-P.; Wu, X.-L. ZnF_2-riched inorganic/organic hybrid SEI: in situ-chemical construction and performance-improving mechanism for aqueous zinc-ion batteries. *Angew. Chem. Int. Ed.* **2023,** *62*, e202216934.

(63) Nie, X.; Miao, L.; Yuan, W.; Ma, G.; Di, S.; Wang, Y.; Shen, S.; Zhang, N. Cholinium cations enable highly compact and dendrite-free Zn metal anodes in aqueous electrolytes. *Adv. Funct. Mater.* **2022,** *32*, 2203905.

(64) Wilson, J. C.; Caratzoulas, S.; Vlachos, D. G.; Yan, Y. Insights into solvent and surface charge effects on Volmer step kinetics on Pt (111). *Nat. Commun.* **2023,** *14*, 2384.

(65) Zeng, X.; Xie, K.; Liu, S.; Zhang, S.; Hao, J.; Liu, J.; Pang, W. K.; Liu, J.; Rao, P.; Wang, Q.; Mao, J.; Guo, Z. Bio-inspired design of an in situ multifunctional polymeric solid-electrolyte interphase for Zn metal anode cycling at 30 mA cm^{-2} and 30 mA h cm^{-2}. *Energy Environ. Sci.* **2021,** *14*, 5947-5957.

(66) Zhu, Q.; Sun, G.; Qiao, S.; Wang, D.; Cui, Z.; Zhang, W.; Liu, J. Selective shielding of the (002) plane enabling vertically oriented zinc plating for dendrite-free zinc anode. *Adv. Mater.* **2023,** *36*, 2308577.

(67) Yang, S.; Chen, A.; Tang, Z.; Wu, Z.; Li, P.; Wang, Y.; Wang, X.; Jin, X.; Bai, S.; Zhi, C. Regulating the electrochemical reduction kinetics by the steric hindrance effect for a robust Zn metal anode. *Energy Environ. Sci.* **2024,** *17*, 1095-1106.

(68) Yuan, W.; Nie, X.; Ma, G.; Liu, M.; Wang, Y.; Shen, S.; Zhang, N. Realizing textured zinc metal anodes through regulating electrodeposition current for aqueous zinc batteries. *Angew. Chem. Int. Ed.* **2023,** *62*, e202218386.

(69) Qiu, M.; Sun, P.; Wang, Y.; Ma, L.; Zhi, C.; Mai, W. Anion-trap engineering toward remarkable crystallographic reorientation and efficient cation migration of Zn ion batteries. *Angew. Chem. Int. Ed.* **2022,** *61*, e202210979.

(70) Ming, F.; Zhu, Y.; Huang, G.; Emwas, A.-H.; Liang, H.; Cui, Y.; Alshareef, H. N. Co-solvent electrolyte engineering for stable anode-free zinc metal batteries. *J. Am. Chem. Soc.* **2022,** *144*, 7160-7170.

(71) Zhu, J.; Bie, Z.; Cai, X.; Jiao, Z.; Wang, Z.; Tao, J.; Song, W.; Fan, H. J. A molecular-sieve electrolyte membrane enables separator-free zinc batteries with ultralong cycle life. *Adv. Mater.* **2022,** *34*, 2207209.

(72) Zeng, Y.; Sun, P. X.; Pei, Z.; Jin, Q.; Zhang, X.; Yu, L.; Lou, X. W. Nitrogen-doped carbon fibers embedded with zincophilic cu nanoboxes for stable Zn-metal anodes. *Adv. Mater.* **2022,** *34*, 2200342.

(73) Li, W.; Zhang, Q.; Yang, Z.; Ji, H.; Wu, T.; Wang, H.; Cai, Z.; Xie, C.; Li, Y.; Wang, H. isotropic amorphous protective layer with uniform interfacial zincophobicity for stable zinc anode. *Small* **2022,** *18*, 2205667.

(74) Hong, L.; Wu, X.; Wang, L.-Y.; Zhong, M.; Zhang, P.; Jiang, L.; Huang, W.; Wang, Y.; Wang, K.-X.; Chen, J.-S. Highly reversible zinc anode enabled by a cation-exchange coating with Zn-ion selective channels. *ACS Nano* **2022,** *16*, 6906-6915.

(75) Li, G.; Zhao, Z.; Zhang, S.; Sun, L.; Li, M.; Yuwono, J. A.; Mao, J.; Hao, J.; Vongsvivut, J.; Xing, L.; Zhao, C.-X.; Guo, Z. A biocompatible electrolyte enables highly reversible Zn anode for zinc ion battery. *Nat. Commun.* **2023,** *14*, 6526.

(76) Feng, D.; Jiao, Y.; Wu, P. Guiding Zn uniform deposition with polymer additives for long-lasting and highly utilized Zn metal anodes. *Angew. Chem. Int. Ed.* **2023,** *62*, e202314456.

(77) Li, H.; Ren, Y.; Zhu, Y.; Tian, J.; Sun, X.; Sheng, C.; He, P.; Guo, S.; Zhou, H. A bio-inspired trehalose additive for reversible zinc anodes with improved stability and kinetics. *Angew. Chem. Int. Ed.* **2023,** *62*, e202310143.

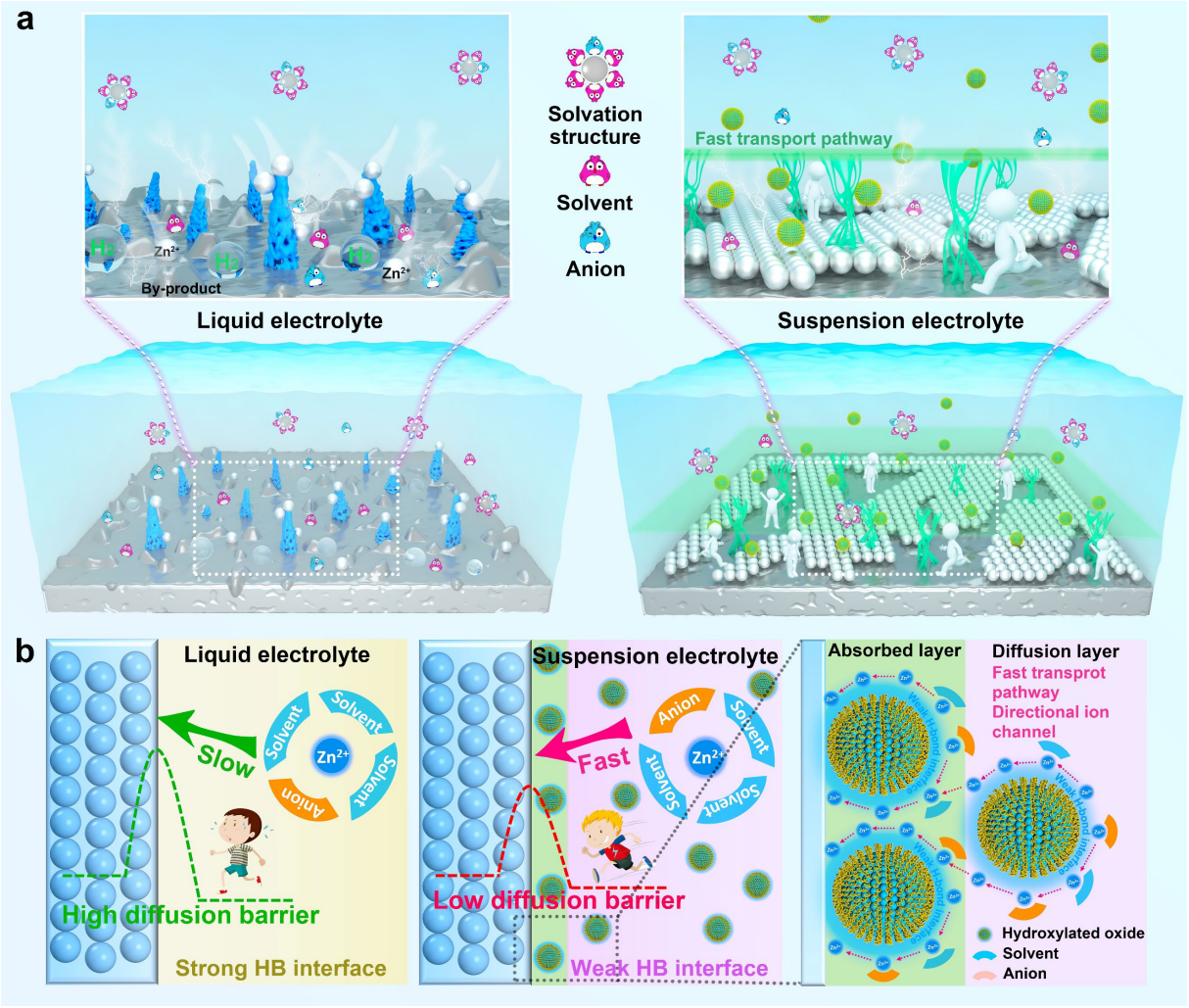

Scheme 1. Illustrations show the Zn deposition behavior on the Zn anode in (a) pure $Zn(OTf)_2$ electrolyte and suspension electrolyte containing TiO_2 nanoparticles with fast transport pathway. (b) Diffusion kinetics in the various electrolytes with strong H-bond interface and weak H-bond interface.

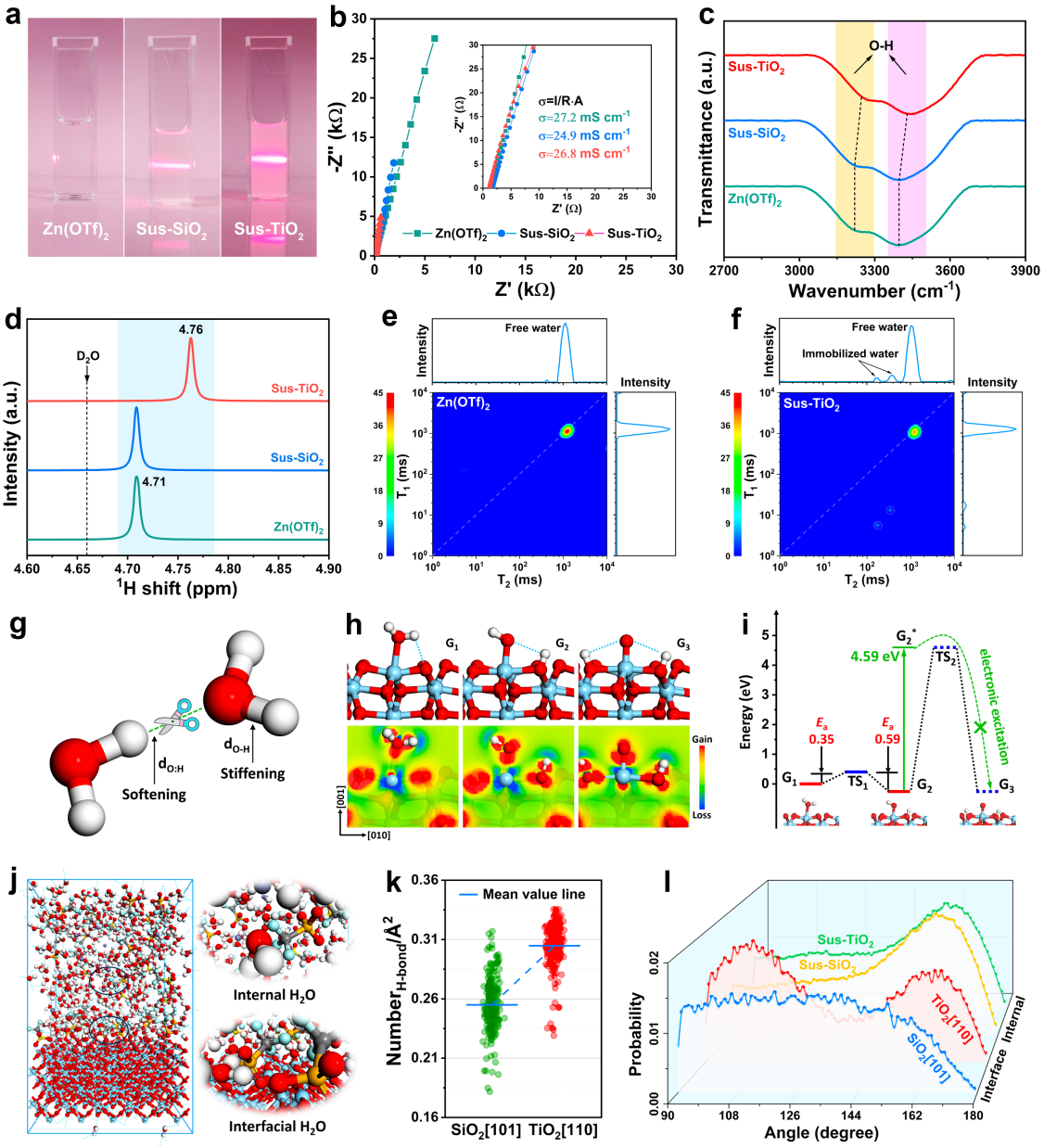

Figure 1. Electrolyte structures and H-bond characterizations of the various electrolytes. (a) Optical images and Tyndall effect of liquid electrolyte and suspension electrolytes with 0.05 *wt*.% nano-oxides. (b) Nyquist impedance plots and the corresponding ionic conductivities. (c) FTIR spectra. (d) ^{1}H NMR spectra. 2D LF-NMR T_1-T_2 relaxation spectra of (e) 3M $Zn(OTf)_2$ and (f) sus-TiO_2 electrolytes. (g) Schematic showing H-bond breakage between two water molecules, resulting in a softening of the O:H bond and stiffening of the O-H bond. (h) Structural geometries and calculated charge difference maps of G_1, G_2, and G_3, respectively. (i) Calculated energy barriers along the dehydrogenation pathways in (h). (j) Snap-shot of MD

simulation of $TiO_{2[110]}$/electrolyte interface, the enlarged images show the internal and interfacial water molecules. (k) The mean values of the H-bond number be-tween oxide lattice planes and water molecules. (l) The probability of H-bond angle.

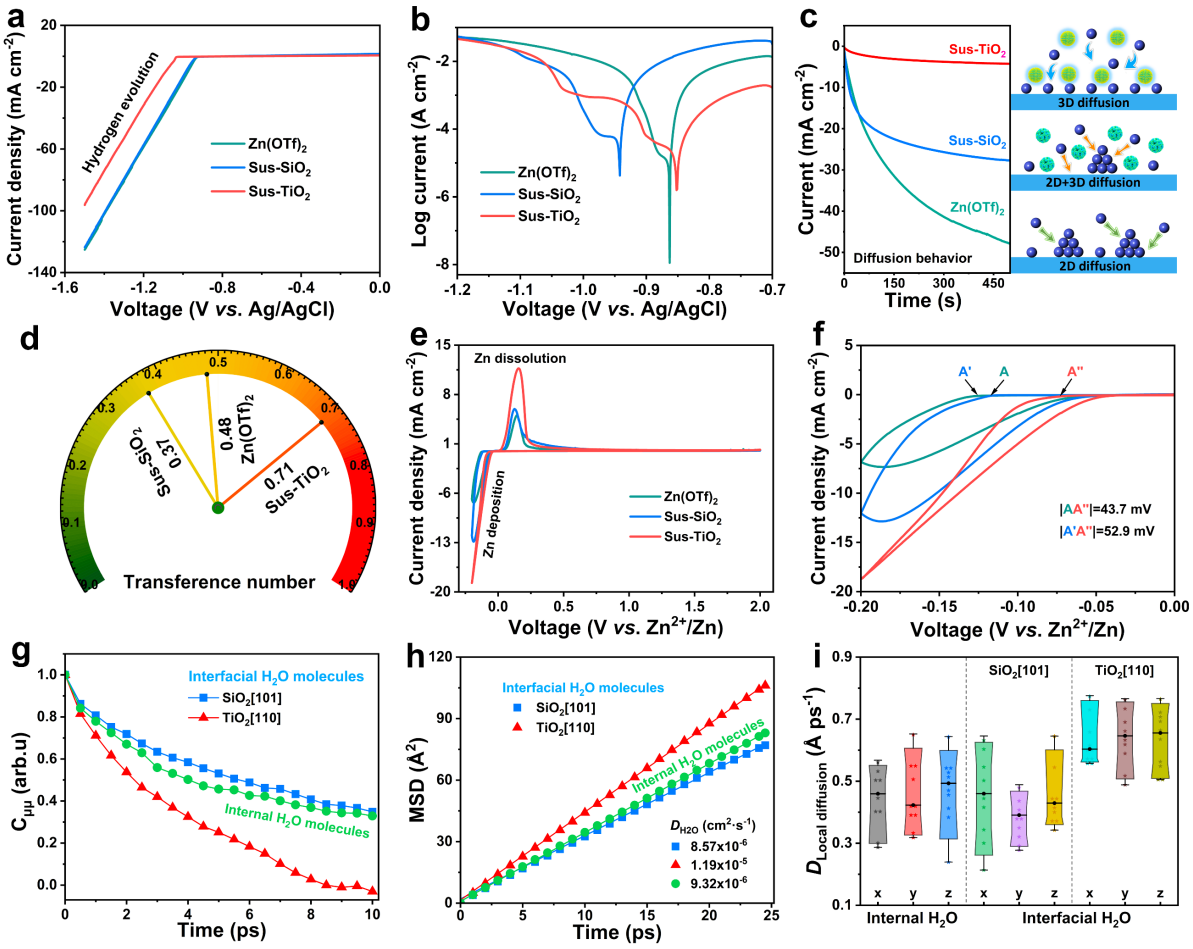

Figure 2. The role of various electrolytes on Zn deposition. (a) LSV curves at 5 mV s^{-1}. (b) Tafel plots of Zn anodes. (c) Chronoamperometric curves of Zn electrodeposition. (d) Zn^{2+} transference number. (e) CV curves of Zn||Ti cells at 5.0 mV s^{-1} (the second cycle) and (f) the partial enlarged view. Dynamic relaxation behaviours for the interfacial and internal water molecules: (g) Dipole vector autocorrelation function (DACF), (h) the simulated MSD *vs*. time curves, and (i) the local diffusion coefficients.

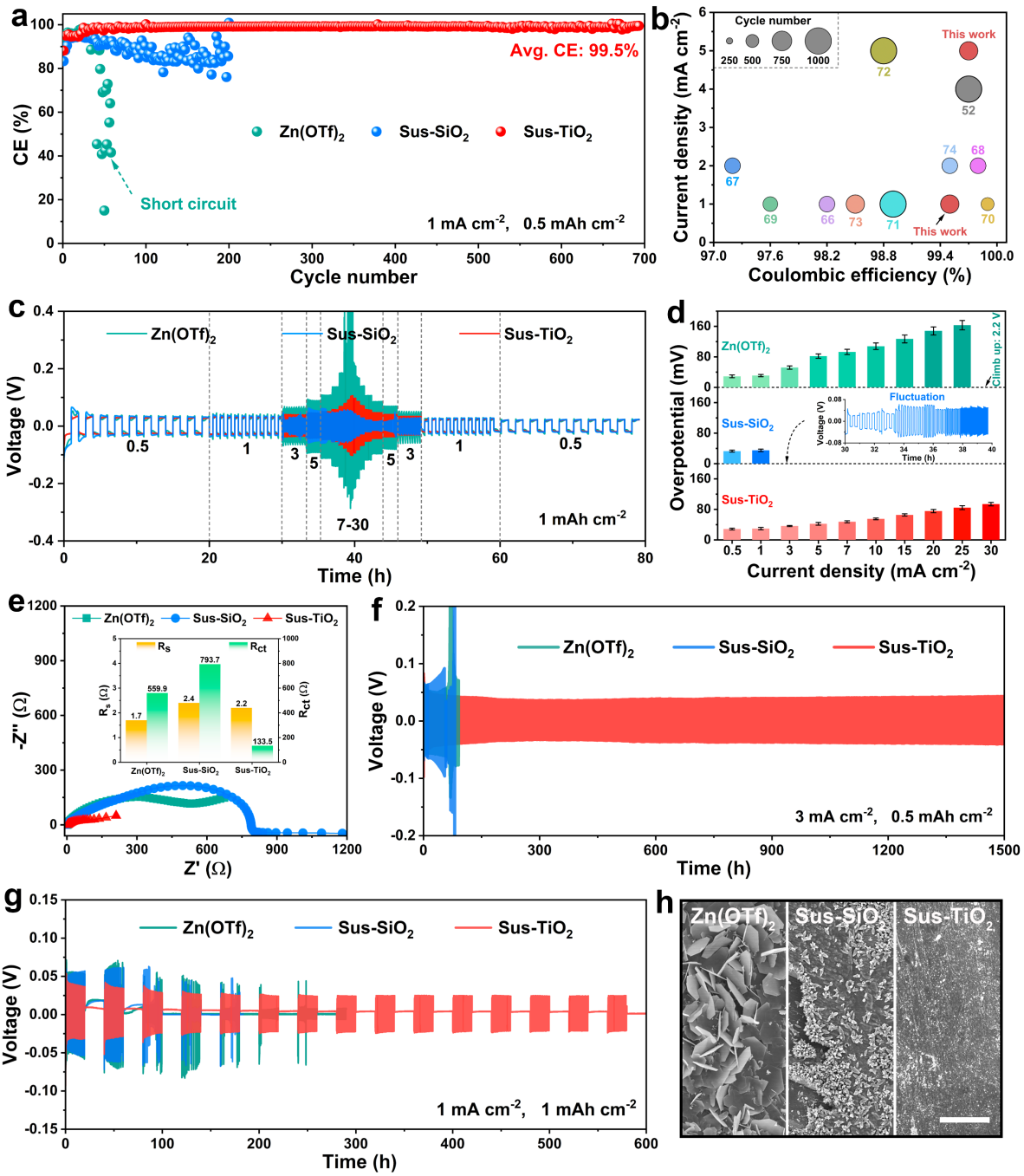

Figure 3. Electrochemical performance of Zn anodes in various electrolytes. (a) CE measurements. (b) Comparisons of CE, cycle number, and current density between this work and recent reported literatures. (c) Rate capability, (d) and the corresponding overpotentials. (e) Nyquist impedance plots after 3 cycles, and the corresponding R_s and R_{ct} values. (f) Cycling performance. (g) Cycling performance during intermittent discharge/charge test. (h) SEM images of Zn anodes after 50 cycles, scale bar: 5 μm.

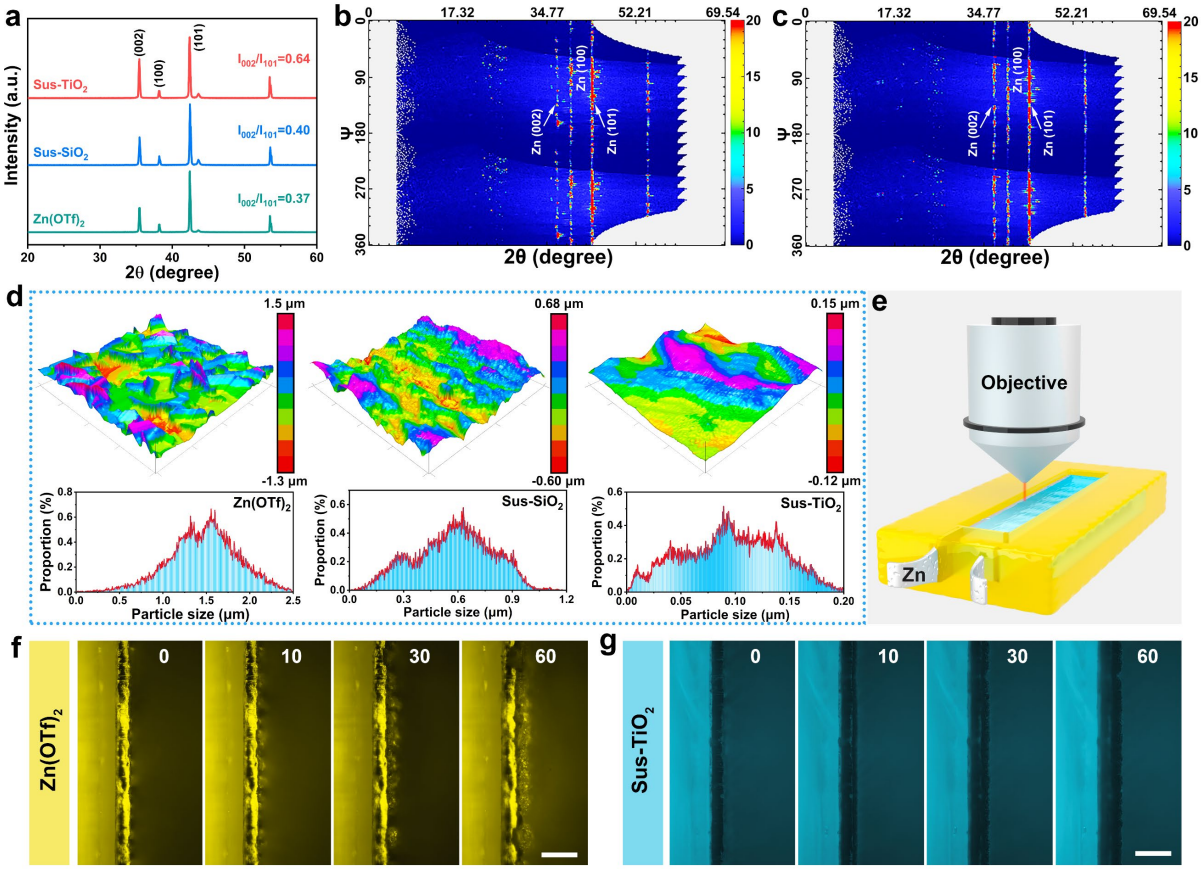

Figure 4. Nucleation and *in-situ* deposition behaviours of Zn in various electrolytes. (a) XRD patterns of the deposited Zn, the corresponding WAXS patterns in (b) $Zn(OTf)_2$, and (c) sus-TiO_2 electrolytes. (d) AFM images and the surface roughness plots of the deposited Zn surface after 50 cycles. (e) Schematic diagram of *in-situ* optical detection platform. *In-situ* optical observation of deposited Zn morphologies in (f) $Zn(OTf)_2$ and (g) sus-TiO_2 electrolytes, scale bar: 100 μm.

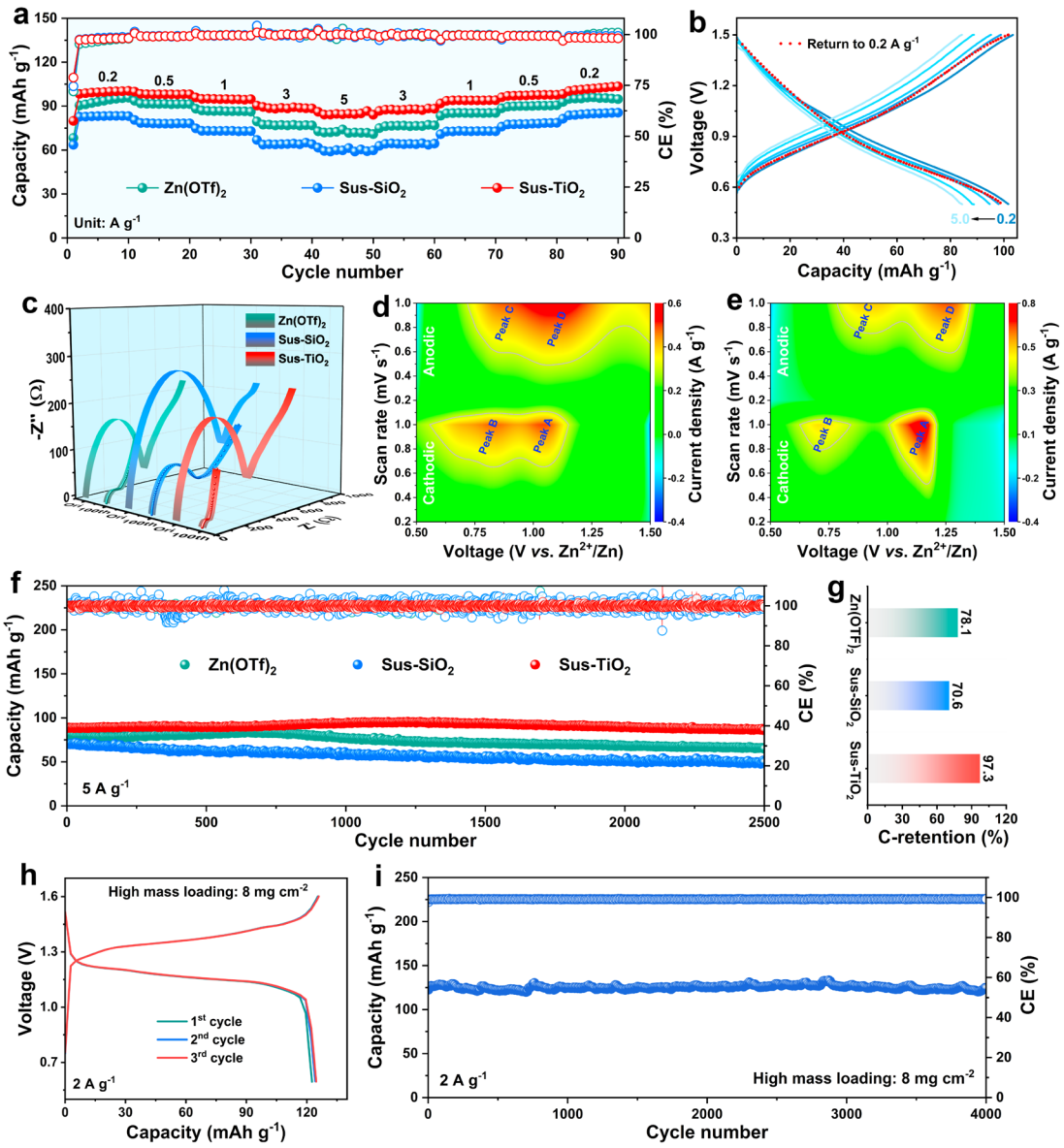

Figure 5. Electrochemical properties of Zn||PANI hybrid capacitors and Zn||ZnVO full batteries in various electrolytes. (a) Rate capability of Zn||PANI hybrid capacitor, and (b) the corresponding discharge/charge curves. (c) Nyquist impedance spectroscopy before and after 100 cycles. 2D contour plots of CV patterns of Zn||PANI hybrid capacitors in (d) $Zn(OTf)_2$ and (e) sus-TiO_2 electrolytes. (f) Cycling stability over 2,500 cycles, and (g) the corresponding capacity retention of Zn||PANI hybrid capacitors. Electrochemical performance of Zn||I_2 full batteries with a high mass loading of ~8.0 mg cm^{-2}: (h) discharge/charge profiles, and (i) cycling stability over 4,000 cycles in the sus-TiO_2 electrolyte at 2.0 A g^{-1}.

A weak H-bond interface with suspension electrolyte is developed to overcome the problems of HER and dendrites on the Zn anode. Such electrolyte possesses low water activity and exhibits high Zn^{2+} transfer kinetics. The resulting Zn||Zn cells and full cells display stable reversibility of Zn plating/stripping behaviors.

Shuai Wang, Haoran Wang, Jiguo Tu, Lei Huang, Shenzhen Deng, Bingang Xu,* and Lei Wei*

Weak H-Bond Interface Environment for Stable Aqueous Zinc Batteries

TOC